Nano Research

Open Access

Research Article

Directly imaging the *in-situ* chemical transformation of nickel cubane nanoclusters for promoting electrocatalytic urea-oxidation-reaction

En-Xue Liu[1,§], Hong-Hao Li[1,§], Cheng Hou[1], Jian-Qiang Zhao[1], Mohamedally Kurmoo[4], Yi-Jing Gao[3] ✉, Zheng Yin[1] ✉, Bin Zhang[1] ✉, and Ming-Hua Zeng[1,2] ✉

[1] *State Key Laboratory for the Chemistry and Molecular Engineering of Medicinal Resources, School of Chemistry and Pharmaceutical Sciences, Guangxi Normal University, Guilin 541004, China*
[2] *Hubei Collaborative Innovation Center for Advanced Chemical Materials, Ministry of Education Key Laboratory for the Synthesis and Application of Organic Functional Molecules and College of Chemistry and Chemical Engineering, Hubei University, Wuhan 430062, China*
[3] *Zhejiang Engineering Laboratory for Green Syntheses and Applications of Fluorine-Containing Specialty Chemicals, Institute of Advanced Fluorine-Containing Materials, Zhejiang Normal University, Jinhua 321004, China*
[4] *Institute de Chimie de Strasbourg, CNRS-UMR7177, Université de Strasbourg, 4 rue Blaise Pascal, Strasbourg 67070, France*
[§] *En-Xue Liu and Hong-Hao Li contributed equally to this work.*

Cite this article: *Nano Research*, **2025**, *18*, 94907152. https://doi.org/10.26599/NR.2025.94907152

ABSTRACT: We report the stepwise *in-situ* manipulation of a nickel cubane nanocluster capped with a specially designed multidentate ligand $[Ni^{II}_4(HL)_3(CH_3O)(CH_3OH)_3](CH_3COO)$ (Ni4, H_3L = (E)-3-((2-hydroxy-3-methoxybenzylidene)amino)propane-1,2-diol) to firstly $[Ni^{II}_4(HL)_3(CH_3O)(CH_3OH)_2(H_2O)](CH_3COO)$ (Ni4-1 min) and finally to $[Ni^{II}_4(HL)_3(CH_3O)(H_2O)_3](CH_3COO)$ (Ni4-20 h) during the urea electrolysis. A combination of mass spectrometry, single crystallography and pair distribution function were employed to analyze the structural correlations of this catalyst in crystal/solution/gas phases for confirming the dynamic ligand replacement while preserving the cubic Ni4 core during catalysis. The key feature of their structures is that: (i) three ligands wrap the Ni_4O_4 cubane center on one side forming the rounded outside of a calix; (ii) the opposite flat side containing labile methanol as the active site. This structure facilitates the binding of the substrate to the active central nickel atoms during catalysis. Furthermore, due to the different modes of packing, the structure of Ni4-20 h sustains two-dimensional (2D) net of open space while the structures of Ni4 and Ni4-1 min have only closed void inaccessible to solvent molecules or ions. Interestingly, the overpotential initially decreased (up to 45 min) until it is stabilized. The result showed a low potential of 1.32 V (urea oxidation reaction (UOR)) at 10 $mA \cdot cm^{-2}$ as reflected in the Gibbs free energy decrease of ~ 0.4 eV from Ni4 to Ni4-20 h. This work demonstrates a convincing approach for elucidating the exact nature of the active clusters in electrocatalytic process, and confirms that *in-situ* modification of electrode materials might alter the direct electronic interaction between substrate and active sites in improving the catalytic performance.

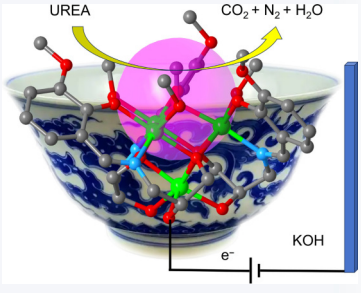

KEYWORDS: atomically precise nanocluster, nickel cubane, electrode modification, urea oxidation reaction

1 Introduction

In the process of chemical reactions, especially in catalytic systems, complex kinetic evolution of active centers always occurs, and the accompanying intermediates and products are undergoing constant transformation and reconstruction [1, 2]. Thus, synthesis nanoplatforms with atomically precise structures and observation of the dynamic structural transformation for manipulating the active sites would provide insights into the understanding of the catalytic process. Currently, *in-situ* or *operando* techniques have emerged as effective tools to monitor the changes of these catalytic processes in real time, and detect the crystalline phase changes, valence changes, and morphology evolution of the catalysts [3–5]. For example, *in-situ* Raman spectroscopy and *in-situ* Fourier transform infrared spectrometer spectroscopy are widely utilized for real-time detection of reaction intermediates, which is more sensitive and accurate that *ex situ* detection [6–8]. *In-situ* transmission electron

Received: October 21, 2024; **Revised:** November 21, 2024
Accepted: November 23, 2024

✉Address correspondence to Ming-Hua Zeng, zmh@mailbox.gxnu.edu.cn; Bin Zhang, binzhang2024@gxnu.edu.cn; Zheng Yin, yinzheng@mailbox.gxnu.edu.cn; Yi-Jing Gao, yijinggao@zjnu.edu.cn

microscope enables real-time monitoring of phase transitions and morphological evolution with temporal resolution at the atomic scale, despite of the harsh demand for tracking reaction process [9–11]. *In-situ* X-ray photoelectron spectroscopy (XPS) or X-ray absorption spectroscopy which can characterize the electronic state variations of catalysts throughout the whole reaction process, helps to further infer the active ingredients in the catalytic system, yet these techniques are limited when applied to liquid phase reactions [12–14]. Over the past decades, electrospray ionization mass spectrometry (ESI-MS) has evolved into a powerful instrumental method to pseudo *in-situ* track the processes of chemical reactions together with pair distribution function (PDF) and single-crystallography for analyzing the structural correlations of crystal/solution/gas phases for solid catalysts [15–21].

As a soft ionization and pseudo real-time monitoring technique, ESI-MS combining with PDF and density function theory (DFT) calculations stands out among various *in-situ* techniques for digging deeper into the solid–liquid phase reaction mechanisms by preserving the intermediates well during in the reaction colloids. Noteworthy, the important premise for accurately studying the catalytic reaction processes is a catalytic platform with identical active sites and consistently well-configured site. Thus, metallic coordination clusters featured with few central metal atoms and organic ligands are good model catalysts for exploring many important chemical processes, benefiting from the advantages of these clusters such as precise atomic numbers, definite compositions, and tunable geometric and electronic structures [22–31]. ESI-MS can collect a large amount of information about the fragmentation pathway of coordination clusters, thus able to track the assembly process of coordination clusters during the synthetic and catalytic reactions [32–37]. In our previous work, ESI-MS has been successfully developed for investigating the cluster formation (Table S1 in the Electronic Supplementary Material (ESM)): (1) using two similar ligands, it was found that the two ligands underwent an *in-situ* competition reaction during the assembly process, forming coordination molecular clusters with different nucleus numbers from a single ligand [38]; (2) by changing the temperature, the ligand undergoes an *in-situ* transformation to form a coordination molecular cluster with a new structure [39]. Among the many coordination clusters, the cubic alkane cluster has attracted much attention because of its good catalytic performance, tunable structure and well-defined composition [18, 21, 40–45]. Moreover, the metal centers in quite a few natural enzymes adopt cubic, like the $[Fe_4S_4]$ cluster in hydrogenase and the oxygen evolution center (OEC) $[Mn_4Ca]$ cluster of photosystem II complex, suggesting the promising potential for cubic alkane clusters as highly active catalysts [46, 47].

Urea oxidation reaction (UOR) is an auxiliary water electrolysis hydrogen production technology developed in recent years aiming at replacing oxygen evolution reaction (OER) and reducing energy consumption. Therefore, UOR can improve hydrogen production efficiency with low theoretical potential and reduce the average cost of electro-chemical hydrogen production. However, UOR requires a complex intermediate adsorption/desorption process, so current research is mainly focused on deciphering its precise reaction mechanism to design more cost-effective and efficient catalysts [48–50]. Our previous working experiences in electrochemistry endow us the platform to gain deep insight into UOR [51–55]. Here, we employed a solvothermal reaction to obtain a precisely-structured, cubic alkane cluster $[Ni_4(HL)_3(CH_3O)(CH_3OH)_3](CH_3COO)$ (Ni4, H_3L = (E)-3-((2-hydroxy-3-methoxybenzylidene) amino)propane-1,2-diol). It is a polar cubic electrocatalyst with a Ni_4O_4 active surface and good UOR activity. Interestingly, the potential of the electrocatalyst deposited on the carbon paper exhibits a rapid decay, reaching equilibrium after about 45 min. In response to this interesting phenomenon, we delve into the dynamics of this catalytic process as well as the structural transformation. Finally, a mechanism is proposed by pseudo *in-situ* tracking the catalytic process of coordination molecular clusters and DFT calculations. The results of this study not only have enlightening significance for investigating the electrocatalytic reactions over organometallic compounds, but also inspire the rational design of coordination molecular cluster catalysts in the future.

2 Results and discussion

2.1 Crystal structures

The key feature of the crystal structure of Ni4 is the cubic Ni_4O_4 center surrounded by three organic ligands donating six bonds each and only one μ_3-OCH_3 at one corner with three symmetrically positioned neighboring terminal methanol (Fig. 1). The cubic molecule is chiral and both enantiomers are present within the achiral unit cell. Each multidentate ligand bridges three nickel atoms of the cubic Ni_4O_4 core in a special conformation μ_3: η^1: η^1: η^1: η^3. Each molecule has the three ligands wrapping the Ni_4O_4 cube about a pseudo C_3 axis shielding its three faces. The face contains the central μ_3-OCH_3 and three methanol also placed nearly symmetric about a pseudo C_3 axis (Tables S2–S4 in the ESM). The ligand and the methanol rotate clockwise and anticlockwise for the respective enantiomers. Interesting to note their disposition around the cube resulted in segregation of an organic shroud and an inorganic surface [56]. The overall shape is like an organic calix with an inorganic cover. This point is important for the electrochemistry that will follow. The molecule finally arranges in this fashion due to the special coordination mode of the ligand. By extending the ligand with the propanediol unit, it affords six bonds with three nickel centers and occupies a corner of the cube with a μ_3-O and bridges two edges. This coordination geometry only permits the packing of three ligands around the cube and forces the clockwise positioning. Consequently, the six missing bonds for all Ni in octahedral geometry are provided by the μ_3-OCH_3 and the three terminal methanol molecules.

At present, most cubane structures use bidentate chelating or

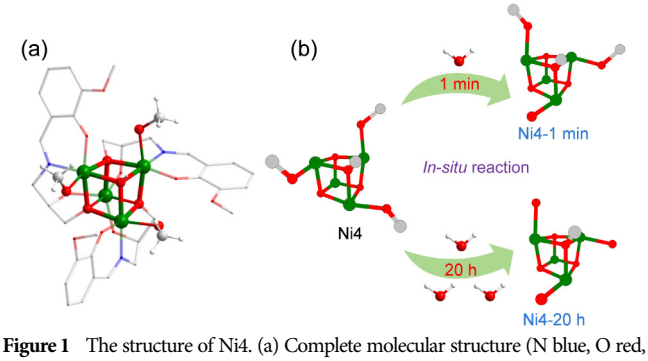

Figure 1 The structure of Ni4. (a) Complete molecular structure (N blue, O red, C gray, Ni green, H white) and (b) *in-situ* transition process from Ni4 to Ni4-1 min and Ni4-20 h, white hydrogen atoms and ligands have been omitted for clarity.

bridging ligands, and generally the catalytic reactions over such cubane clusters were carried out in a mild environment due to the unsatisfactory stability in harsh environments [57]. Considering that certain unpredictable structural changes might occur during the cluster preparation and electrocatalytic process, precise control of the surface structure of the catalyst to improve its catalytic activity remains a key challenge. Fortunately, the skeleton of Ni4 retains the cubic Ni_4O_4 core structure during the electrolysis process, and two types of *in-situ* modified structures were obtained named by Ni4-1 min and Ni4-20 h. The difference between Ni4-1 min and Ni4-20 h and Ni4 is that the one methanol molecule is replaced by one water molecule in the former and all three methanol molecules are replaced by water molecules in the latter (Fig. S2 in the ESM). In addition, it is demonstrated for the first time by diffraction of single crystals that the cluster retains its crystalline structure after catalysis. Although the space group has changed of 1 min and Ni4-20 h, this change has also led to an improvement in the catalytic process and an increase in catalytic effect.

Comparing the three structures, apart from the space groups, the packing is very different. The structure of Ni4 is relatively compact, with large cluster-to-cluster interactions, so that one of them presents closed pockets in the *b*–*c* direction with a porosity of 13.0%, and such closed pores are not accessible to solvents. As the catalytic reaction proceeds, the structure of Ni4 undergoes an *in-situ* transformation ligand methanol is gradually replaced by water，Ni4-1 min has one-dimensional channels with a porosity of 17.0%，these channels are constricted and also hard to accessible (Figs. 2(a) and 2(b)). When the reaction reaches a certain level, all the methanol was replaced by water, two-dimensional (2D) penetrating pore channels with a porosity of 32.6% appeared in Ni4-20 h (Fig. 2(c)), allowing good access to the reactant. Consequently, the replacement of methanol by water relieves the steric hindrance and facilitates the easy access of urea to the electroactive surface for the UOR. At the same time, it can also be seen from the three-dimensional structure packing diagram that the Ni4-1 min and Ni4-20 h are looser, increasing the contact between the substrate and the active site is also conducive to efficient catalysis (Fig. S3 in the ESM). Such *in-situ* modifications can expose more reactive surface sites and promote efficient electron transfer behavior.

The cubane backbone of the catalyzed sample and the coordination mode of the ligand remain unchanged. This confirms the hypothesis concerning the stability before and after catalysis and the reaction is favored on the surface containing the labile solvents—the inorganic face of the molecular cluster. In order to further prove the structural stability, we found that Ni4 clusters always maintain the stability of the frame peak under the conditions of mass spectrometry. A surprising finding is that several peak changes were observed after catalysis, reflecting the dynamic changes during the catalysis process (see below). The powder X-ray diffraction (PXRD) pattern of Ni4 matches well the simulated pattern derived from the single-crystal structure data and its thermogravimetric analysis (TGA) shows loss of the coordinated methanol in step of one at a time (Figs. S4 and S5 in the ESM).

2.2 Electrochemical properties

A typical three-electrode setup was used to survey the electrocatalytic performance of the Ni4 catalyst. In order to make a direct comparison to previous studies, the electrolyte 1 M KOH and 0.33 M urea were selected for evaluating the UOR activity, and compared the UOR performance of Ni4 with common catalysts：$Ni(OH)_2$， RuO_2 under the same catalytic conditions in the same preparation. The linear sweep voltammetry (LSV) curve with Ni4 electrode exhibits an overpotential of 1.32 V to reach a current density of 10 mA·cm^{-2}, compared to OER, the UOR plot exhibits a rapidly rising anodic current density, this potential is reduced by 210 mV (Fig. 3(a)). UOR activity outperformed RuO_2 and $Ni(OH)_2$ demonstrating a better UOR catalytic activity. Furthermore, the Ni4 exhibits a distinctly higher current density (314 mA·cm^{-2}) than other control samples, further demonstrating high catalytic activity (Fig. 3(b)). To explore the reaction kinetics of Ni4 catalyst the corresponding Tafel slope derived from their UOR polarization curves are presented. Tafel slopes for a Ni4 electrode was ca. 32.4 mV·dec^{-1} which is again lower than those of RuO_2 (141.5 mV·dec^{-1}) and $Ni(OH)_2$ (40.1 mV·dec^{-1}), suggesting the Ni4 catalyst is kinetically efficient (Fig. 3(c)), suggesting the Ni4 catalyst the optimal adsorption characteristics and rapid reaction kinetics for the urea molecules. Electrochemical impedance spectroscopy (EIS) measurement was also carried out to deeply explore the UOR kinetics of these catalysts. It is revealed that the Ni4 has the smallest charge transfer resistance (R_{ct}), i.e., 3.22 Ω, which is consistent with its smallest Tafel slope and further demonstrates its rapid UOR kinetics (Fig. 3(d)), and it should be noted that these values are beneficial in promoting electrocatalytic reactions. The above results indicated that Ni4 has excellent electrocatalytic performance, which is comparable to the state-of-the-art UOR electrocatalysts, further suggesting the potential of the Ni4 for the use in practical applications. (Fig. S6 and Tables S5–S7 in the ESM). Furthermore, the cyclic voltammetry and chronopotentiometry measurement displayed electrochemical stability. Ni4 showed only a slight potential degradation after 1000 continuous cyclic voltammetry (CV) cycles, further verifying its excellent stability (Fig. 3(e)). In

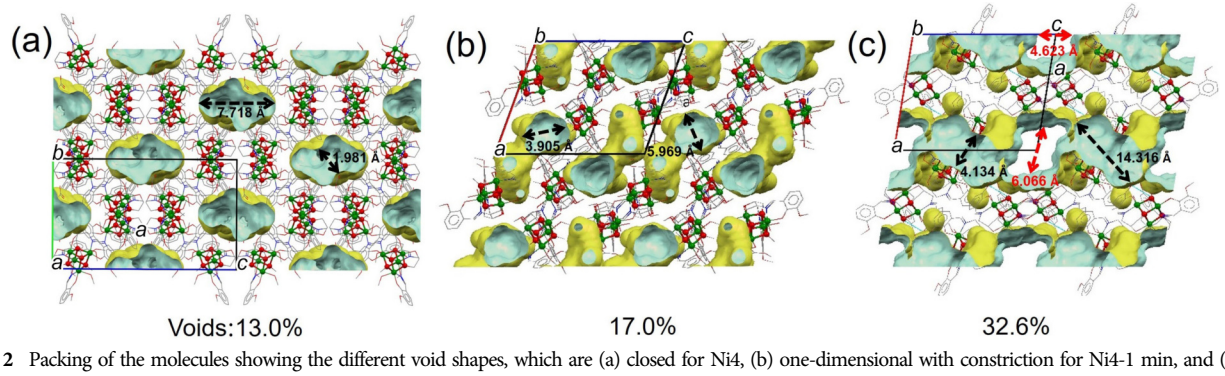

Figure 2 Packing of the molecules showing the different void shapes, which are (a) closed for Ni4, (b) one-dimensional with constriction for Ni4-1 min, and (c) two-dimensional net for Ni4-20 h.

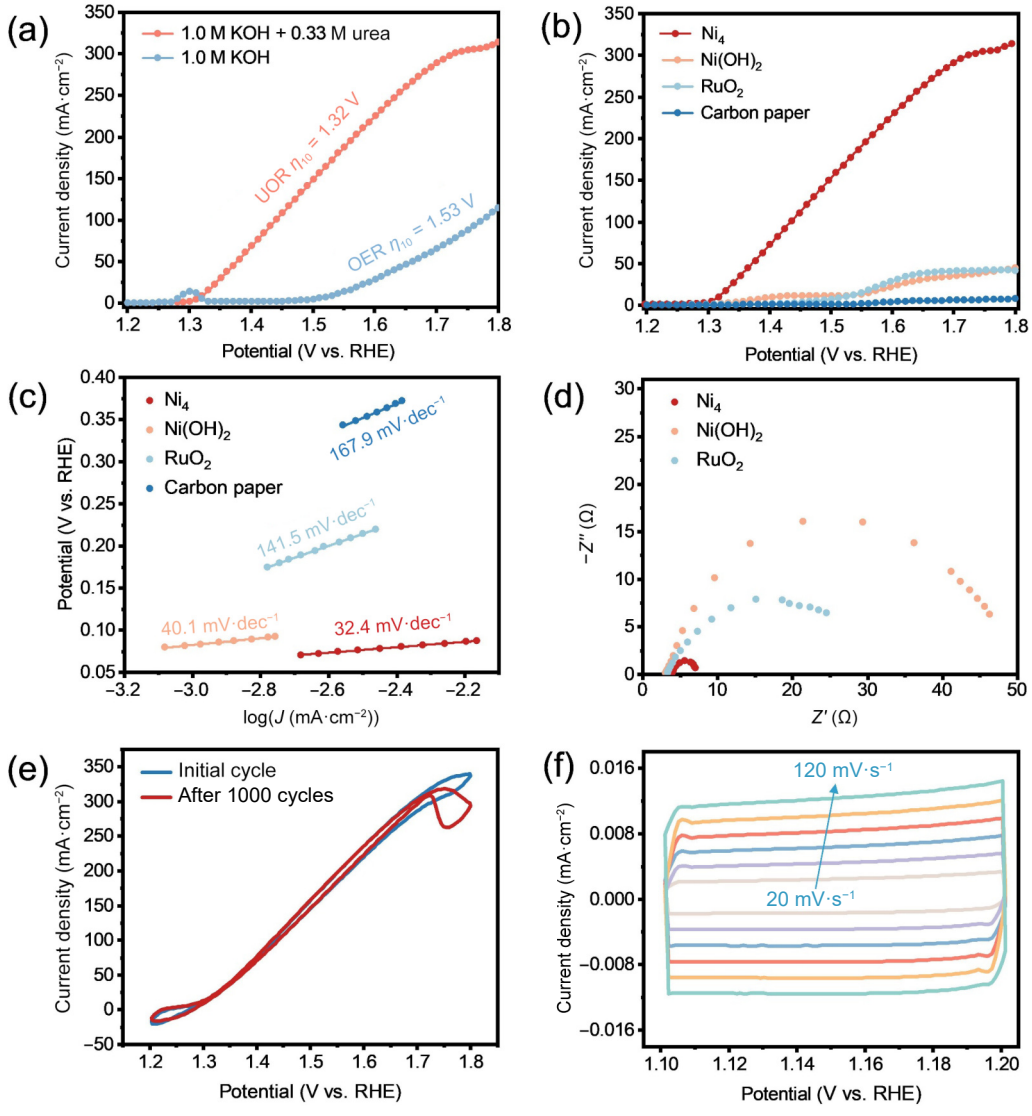

Figure 3 Electrochemical properties of Ni4 on carbon paper: (a) UOR in 1.0 M KOH + 0.33 M urea and OER in 1.0 M KOH of Ni4. (b) LSV curves of Ni4, RuO_2, $Ni(OH)_2$ and carbon paper in UOR. (c) Tafel plots of Ni4, RuO_2, $Ni(OH)_2$ and carbon paper in UOR. (d) Nyquist plots for Ni4, RuO_2 and $Ni(OH)_2$. (e) Durability test—1st versus 1000th cycle of Ni4. (f) The ECSA of Ni4.

general, the larger the electrochemical active surface area (ECSA) (Fig. 3(f)), the more sites are thought to be exposed and the more efficient is the catalytic activity. The ECSA of a catalyst is evaluated by the double-layer capacitance (C_{dl}) (Fig. S7 in the ESM), the C_{dl} was obtained by linearly fitting the current density difference from the cyclic voltammetry curves measured at different scan rates and the date is 0.098 mF·cm^{-2}.

When we did the chronopotentiometry (C-P) test, we found one surprising observation that the rapid decay of the potential started within the first few minutes for all the electrode samples examined. The potential decays to a minimum after a period of about 1 h with a slight variation between samples. Analysis of the data up to this point shows excellent fit to two rates averaging 9 ± 1 V·min^{-1} for the rapid process and 1.1 ± 0.1 V·min^{-1} for the moderate one for a set of six samples. Measured at fixed temperature of 30 °C (Fig. 4). Decay in potential has been observed in a previous study but not specially discussed [58]. Under long-term durability studies, the Ni4 catalyst shows stable potential from 2 to 24 h at a current density of 10 mA·cm^{-2} (Fig. 4). The results indicate that the Ni4 is excellently suited for UOR in alkaline media. This process also confirmed that Ni4 had undergone *in-situ* modification.

2.3 Electrospray ionization mass spectrometry

ESI-MS of Ni4 dissolved in methanol showed abundant fragment variations, and analyses revealed that they were all framework peaks of Ni4 and its ion peak fragments with substitution changes in coordination solvent molecules (Fig. 5 and Fig. S8 in the ESM). The MS spectra of the solution were obtained in positive mode under an insource energy of 0 eV. It exhibits the main ion $[Ni_4(HL)_3(CH_3O)(CH_3OH)_3]^+$, mass-to-charge ratio ($m/z$) = 1030.09. The peaks at m/z = 998.07, 966.04 and 934.01, assigned to progressive loss of methanol, *viz.* $[Ni_4(HL)_3(CH_3O)(CH_3OH)_2]^+$, $[Ni_4(HL)_3(CH_3O)(CH_3OH)]^+$ and $[Ni_4(HL)_3(CH_3O)]^+$. Furthermore, the relative intensities of the fragment peaks were 0.93, 0.30 and 0.11, respectively, which are higher than those of other fragment peaks, indicating that the elimination reaction of coordination methanol molecules was easy to occur (Table S8 and Fig. S9 in the ESM). The fragment peak at m/z = 901.99 is

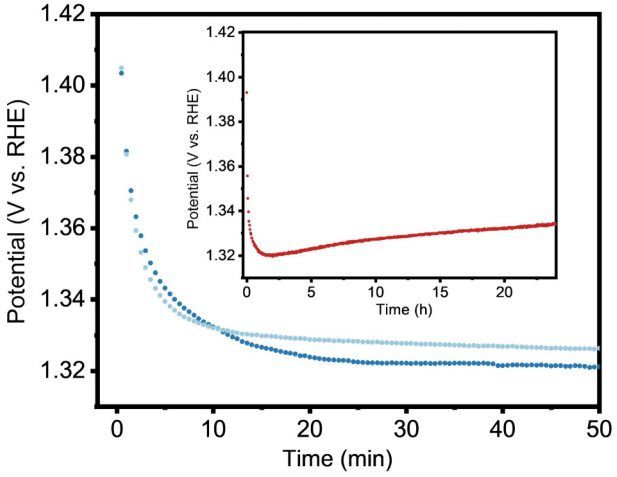

Figure 4 Chronopotentiometry for two different virgin electrodes of Ni4 in 1.0 M KOH and 0.33 M urea showing the initial degradation in potential to stabilization after ca. 45 min. The curves were fitted to the sum of two exponential decays. Inset: chronopotentiometry for a third sample for up to 24 h.

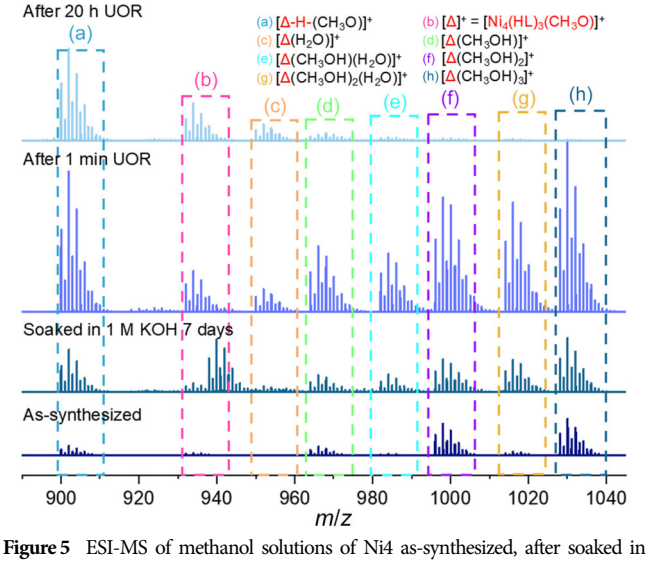

Figure 5 ESI-MS of methanol solutions of Ni4 as-synthesized, after soaked in 1 M KOH for 7 days, after 1 min UOR and after 20 h UOR.

attributed to $[Ni_4(HL)_2(L)]^+$; it is formed by the deprotonating HL^{2-} to L^{3-} and the loss of a methoxy group in the case of further ionization, but the configuration of "Ni_4L_3" is not disrupted. A similar phenomenon can be observed in the ESI-MS in negative mode. Interestingly, a dimerized Ni4 to Ni8 fragment was observed as the singly charged ions $[Ni_8(HL)_3(L)_3]^+$ m/z = 1804.97, $[Ni_8(HL)_3(L)_3(CH_3OH)]^+$ m/z = 1838.00 and $[Ni_8(HL)_3(L)_3(CH_3OH)_2]^+$ m/z = 1869.02. In the negative mode, we can also observe that the Ni4 cube is stable (Fig. 5 and Fig. S8 in the ESM).

Stability of the electrocatalyst is the most important prerequisite for tracking a catalytic reaction. To analyze the stability of Ni4 from the perspective of simulated catalytic conditions, we soaked the samples in 1 M KOH solution for one week, followed by ESI-MS and PXRD characterization analyses (Table S8 and Fig. S10 in the ESM). A surprising finding is that several peaks at m/z 901.99, 952.02, 984.04 and 1016.07 were observed corresponding to $[Ni_4(HL)_2(L)]^+$, $[Ni_4(HL)_3(CH_3O)(H_2O)]^+$, $[Ni_4(HL)_3(CH_3O)(CH_3OH)(H_2O)]^+$ and $[Ni_4(HL)_3(CH_3O)(CH_3OH)_2(H_2O)]^+$, respectively. All MS peaks were associated with fragments containing the entire Ni_4O_4 core is a good indication for its high stability.

In order to verify the structural stability of Ni4 after electrocatalysis, we collected samples and dissolved them in CH_3OH for mass spectrometry at 0 eV. New peaks of different masses appeared compared to those observed for single crystal of Ni4 mass spectrometry (Table S9 in the ESM). The peaks that appeared could be attributed to the framework peaks of Ni4 but the difference is in the relative intensities. We assign the peaks at m/z = 901.99, 934.01, and 952.02 to $[Ni_4(HL)_2(L1)]^+$, $[Ni_4(HL)_3(CH_3O)]^+$, and $[Ni_4(HL)_3(CH_3O)(H_2O)]^+$, respectively, and their relative intensities were greatly improved compared to those of the single crystal Ni4 mass spectrometry, indicating that the departure and replacement of methanol as a coordination solvent molecule are easy to occur in the electrocatalytic process. Based on the scanning electron microscopy (SEM) images, it can be found that Ni4 is more uniformly loaded onto the carbon paper, and that the morphology of the structure before and after the catalytic process does not change obviously, which proves that Ni4 is firmly fixed on the carbon paper during the catalytic process and has a good catalytic stability (Fig. S11 in the ESM). The electronic states before and after catalysis by Ni4 were analyzed by XPS. For the Ni 2p spectra of Ni4, two peaks at 855.1 and 872.8 eV corresponded to Ni $2p_{3/2}$ and Ni $2p_{1/2}$ of Ni^{2+}, respectively, and the other two peaks at 860.6 and 878.3 eV were the corresponding satellite peaks (marked by Sat.). For the spectrum of post-catalyzed Ni 2p, two peaks at 855.3 and 873.1 eV correspond to Ni $2p_{3/2}$ and Ni $2p_{1/2}$ of Ni^{2+}, respectively, and the other two peaks at 861.2 and 878.5 eV are the corresponding satellite peaks. It is demonstrated that Ni4 is divalent before and after catalysis (Fig. S12 in the ESM).

As a heterogeneous catalyst, whether Ni4 can be loaded on carbon paper without dissolution during the catalytic process is also an important reference standard for the stability of Ni4. We employed dichloromethane to extract the electrolyte before and after electrolysis, and ESI-MS to search for the presence of Ni4 or its fragments (Fig. S13 in the ESM). No peak corresponding to Ni4 or its fragments was observed in either case confirming the original catalyst was neither dissolved nor dissociated during electrolysis, demonstrating that Ni4 was securely supported on the carbon paper. Also, we successfully recovered the cluster from the carbon paper using methanol/acetonitrile to crystallize Ni4-1 min and Ni4-20 h, which confirmed that the method of depositing is quite safe for securing Ni4 on the surface.

2.4 Pair distribution function

Comparing the PDF data before and after catalysis, it is found that there is basically no change in the peak position before 6 Å. The observed local correlation for Ni–N/O (2 Å), Ni–Ni (3 Å) and Ni–C (4.8 Å) indicates the atoms maintained their relative arrangement surrounding the nickel center (Figs. 6(a) and 6(b)). However, other peaks in 8–15 Å cannot be clearly assigned, indicating that the packing of molecular clusters changed after catalysis as evidenced by the crystal structures of Ni4-1 min and Ni4-20 h. It is worth noting that the Ni–Ni peak at 3 Å was maintained before and after the catalysis, confirming the well-preservation of the Ni4 core in the structure. The cube structure remained unchanged, indicating that Ni4 is quite stable under the harsh electrochemical environment.

The above results illustrate the dynamic ligand substitution of this cluster maintained the original Ni4 core structure, which inspires us to explore whether the catalytic reaction pathways will

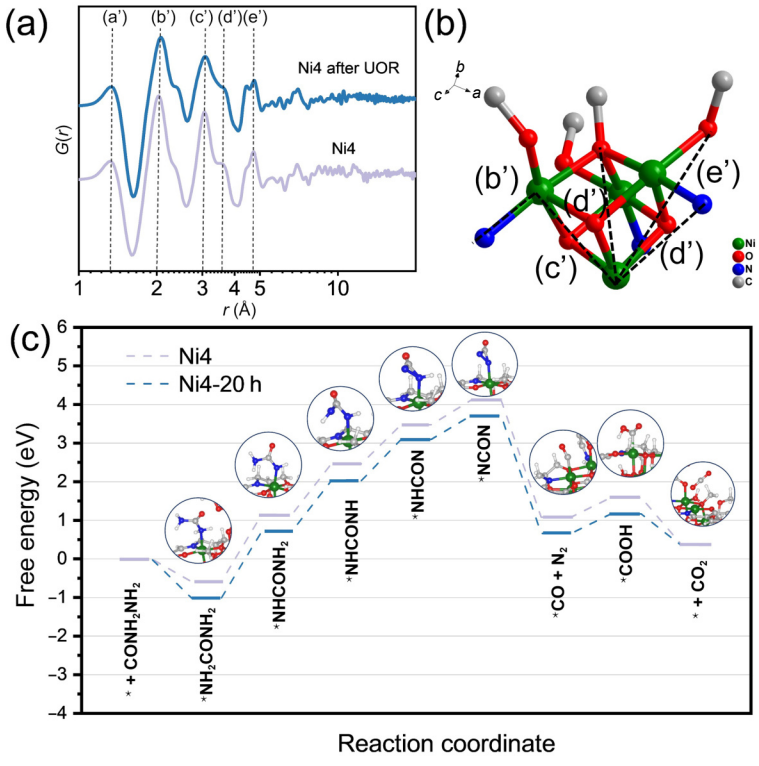

Figure 6 (a) PDF comparison before and after Ni4 catalysis. (b) Interatomic distances of Ni_4O_4 cubane core. (c) The calculated free energy for urea oxidation reaction.

change with the identical central structure but different ligands from the molecular level with theoretical calculations.

2.5 Computational investigation of the mechanism

Since UOR involves a six-electron transfer process, this reaction is related to the formation of multiple intermediates, the adsorption of urea molecules, and the desorption of CO_2 (Table S10 in the ESM). In order to gain an insight into the different operating potentials for Ni4 and Ni4-20 h, we have calculated the free energies of interaction with urea for a sequence of steps during its conversion in the UOR process to CO_2 (Fig. 6(c) and Figs. S14–S16 in the ESM). For the initial step, $CO(NH_2)_2$ activation was investigated with $-NH_2$ terminal, –O terminal and –C terminal. The energy results indicate $CO(NH_2)_2$ favors adsorption on the μ_3 site with $-NH_2$ terminal (−1.63 eV). Other related intermediates adsorption such as $NHCONH_2$, NHCON with different configurations was also investigated. Based on the optimal structure of reactants and intermediates, four reaction pathways were analyzed by Gibbs free energy calculations [59–62]. The reaction pathway includes a proton-coupled electron transfer and hydration. The calculated energies (ΔG in brackets) suggest $*NH_2CONH_2$ is easily oxidized to generate $*NHCONH_2$ (1.71 eV) rather than hydrated to $*NH_2CONH_2(OH)$ (2.85 eV). $*NHCONH_2$ can be further oxidized to *NHCONH (1.33 eV) or $*NCONH_2$ (1.93 eV). $*NCONH_2$ oxidizes to *NCONH (0.81 eV), while *NHCONH oxidizes to *NCONH (1.42 eV) or *NHCON (1.07 eV). Both *NCONH and *NHCON could form $*N_2CO$ through intramolecular coupling. $*N_2CO$ could generate N_2 and CO by rearrangement with −3.05 eV. Similarly, $*N_2CO$ could hydrate into $*N_2CO(OH)$ (−1.01 eV). Subsequently, *COOH and CO_2 are generated through oxidative dehydrogenation. Therefore, the most possible pathway of UOR over this catalyst was proposed to be $*NH_2CONH_2$ → $*NHCONH_2$ → *NHCONH → *NHCON → $*N_2CO$ → *CO → *COOH → $*CO_2$. The free energy results and related structures of intermediates were displayed. The formation of the $*NHCONH_2$ is found to be the potential-determining step with the ΔG of 1.71 eV. In order to compare the same calculation process for Ni4 through theoretical calculations (Figs. S17–S19 in the ESM), we found that the urea adsorption of Ni4-20 h (−1.63 eV) was energetically favorable over Ni4 (−1.20 eV), which was most likely due to the change of stacking mode between cluster nuclei after structural transformation. We note the difference in potentials between the two species is maintained through all the steps. Noteworthy, only negligible difference in the energy barrier of the rate-determining step was detected between Ni4-20 h and Ni4, which may be ascribed to the fact that the active centers are well-preserved during the self-modification process of converting the three-coordinated methanol on the cluster nucleus to the three-coordinated water. Thus, we conclude that ligand engineering altering the absorption energetic profiles of the substrate plays a key role in promoting UOR. Compared to previous studies on UOR catalytic systems which reported the same potential-determining step, Ni_4O_4 cubane system has lower thermodynamic energy barrier [59, 60]. Therefore, it can be conjectured that the low-valent Ni(II) center stabilizes the $*NHCONH_2$ adsorption and the hydrogen bonding effect of the ligand facilitates the urea molecule decomposition, which provides the driving force for the overall catalytic cycle.

3 Conclusions

In dealing with the generally unsatisfactory stability issue for metal cubane nanoclusters, we specially designed a novel multidentate capping ligand, (E)-3-((2-hydroxy-3-methoxybenzylidene) amino)propane-1,2-diol, and synthesized a cubic Ni_4O_4-centered calix-shaped cluster via the unique coordination mode with this ligand which preserves its central structure during electrocatalysis in

alkali conditions. This cluster contains only three ligands, forming an isolated organic shield that shields the outside while the top Ni_4O_4 inorganic surface remains open, ensuring both the stability of the cubane and its efficient UOR electrocatalytic activity, with an overpotential as low as 10 mA·cm^{-2} at 1.32 V. To dig into the reaction mechanism, the evolution of the as-synthesized Ni cluster was analyzed in terms of the structural correlations of crystal/solution/gas phases, which demonstrates that water molecules on the inorganic surfaces progressively replaced one methanol molecule coordinated with the cluster in a short period of time, and all three coordinated methanol molecules in a longer period of time with a combination of ESI-MS, single crystallography, PDF and DFT calculations. The *in-situ* structural change of the gradual ligand substitution, which is also reflected in the rapid decay of the potential in the C-P test, induces changes in the cluster packing and introduces void channels in the final product, thus increasing the surface accessibility. Theoretical simulations indicated a single site mechanism for the UOR reaction, explaining the high catalytic efficiency and admirable stability. This work provides an inspiring approach on how to design ligands that can contribute to the fabrication of structurally well-defined and catalytically efficient electrode materials for future producing UOR. Importantly, the observation of this molecular *in-situ* electrode modification via multi-phase structural correlation characterization in the chemical conversion of urea offers a significant insight in dynamic catalysis, which is crucial for the development of future energy-efficient catalysts.

Electronic Supplementary Material: Supplementary material (crystallographic data, PXRD patterns, TGA curves, ESI-MS spectra and assignments, SEM images, XPS images, and DFT) is available in the online version of this article at https://doi.org/10.26599/NR.2025.94907152.

Data availability

All data needed to support the conclusions in the paper are presented in the manuscript and the Electronic Supplementary Material. Additional data related to this paper may be requested from the corresponding author upon request.

Acknowledgements

We acknowledge the grants from the BAGUI talent program in Guangxi Province (No. 2019AC26001) and the National Natural Science Foundation of China (Nos. 22171075 and U23A2080).

Declaration of competing interest

All the contributing authors report no conflict of interests in this work.

Author contribution statement

M.-H. Z. conceived the idea, co-wrote the paper and supervised the whole experimental procedure and data analysis. M. K., B. Z., Z. Y., and Y.-J. G. edited the manuscript. E.-X. L., H.-H. L., J.-Q. Z., and C. H. performed experiments, analyzed the data and wrote the manuscript. All the authors discussed the results, commented on and revised the manuscript.

Use of AI statement

None.

References

[1] He, Y. Z.; Liu, S. S.; Wang, M. F.; Cheng, Q. Y.; Ji, H. Q.; Qian, T.; Yan, C. L. Advanced *in situ* characterization techniques for direct observation of gas-involved electrochemical reactions. *Energy Environ. Mater.* **2023**, *6*, e12552.

[2] Zhao, J. Y.; Lian, J.; Zhao, Z. X.; Wang, X. M.; Zhang, J. J. A review of *in-situ* techniques for probing active sites and mechanisms of electrocatalytic oxygen reduction reactions. *Nano-Micro Lett.* **2023**, *15*, 19.

[3] Chen, Z. K.; Fan, Q. Q.; Zhou, J.; Wang, X. K.; Huang, M. H.; Jiang, H. Q.; Cölfen, H. Toward understanding the formation mechanism and OER catalytic mechanism of hydroxides by *in situ* and *operando* techniques. *Angew. Chem., Int. Ed.* **2023**, *62*, e202309293.

[4] Li, X. N.; Yang, X. F.; Zhang, J. M.; Huang, Y. Q.; Liu, B. *In situ*/*operando* techniques for characterization of single-atom catalysts. *ACS Catal.* **2019**, *9*, 2521–2531.

[5] Zhao, Y. G.; Adiyeri Saseendran, D. P.; Huang, C.; Triana, C. A.; Marks, W. R.; Chen, H.; Zhao, H.; Patzke, G. R. Oxygen evolution/reduction reaction catalysts: From *in situ* monitoring and reaction mechanisms to rational design. *Chem. Rev.* **2023**, *123*, 6257–6358.

[6] Jing, C.; Yuan, T. T.; Li, L. L.; Li, J. F.; Qian, Z. X.; Zhou, J.; Wang, Y. F.; Xi, S. B.; Zhang, N.; Lin, H. J. et al. Electrocatalyst with dynamic formation of the dual-active site from the dual pathway observed by *in situ* Raman spectroscopy. *ACS Catal.* **2022**, *12*, 10276–10284.

[7] Yoo, R. M. S.; Yesudoss, D.; Johnson, D.; Djire, A. A review on the application of *in-situ* Raman spectroelectrochemistry to understand the mechanisms of hydrogen evolution reaction. *ACS Catal.* **2023**, *13*, 10570–10601.

[8] Zhang, H. Y.; Gu, C. Y.; Fan, M. H.; Zhao, Z.; Kong, X. D.; Geng, Z. G. Applications of *in-situ* spectroscopic techniques towards CO_2 electroreduction. *Sci. China Chem.* **2024**, in press, DOI: 10.1007/s11426-024-2113-7.

[9] Heidari, S. M.; Balaghi, S. E.; Sologubenko, A. S.; Patzke, G. R. Economic manganese-oxide-based anodes for efficient water oxidation: Rapid synthesis and *in situ* transmission electron microscopy monitoring. *ACS Catal.* **2021**, *11*, 2511–2523.

[10] Ma, X. C.; Dong, D. R.; Guo, S. Q.; Cheng, N. Y.; Zhang, B. W.; Ge, B. H. *In situ* transmission electron microscopy for sodium batteries. *Adv. Funct. Mater.* **2024**, *34*, 2400779.

[11] Sun, Z. F.; Pan, J. H.; Chen, W. W.; Chen, H. Y.; Zhou, S. H.; Wu, X. Y.; Wang, Y. S.; Kim, K.; Li, J.; Liu, H. D. et al. Electrochemical processes and reactions in rechargeable battery materials revealed via *in situ* transmission electron microscopy. *Adv. Energy Mater.* **2024**, *14*, 2303165.

[12] Barawi, M.; Mesa, C. A.; Collado, L.; Villar-García, I. J.; Oropeza, F.; de la Peña O'Shea, V. A.; García-Tecedor, M. Latest advances *in situ* and *operando* X-ray-based techniques for the characterisation of photoelectrocatalytic systems. *J. Mater. Chem. A* **2024**, *12*, 23125–23146.

[13] Chetyrin, I. A.; Bukhtiyarov, A. V.; Prosvirin, I. P.; Bukhtiyarov, V. I. Investigation of concentration hysteresis in methane oxidation on bimetallic Pt–Pd/Al_2O_3 catalyst by *in situ* XPS and mass spectrometry. *Mendeleev Commun.* **2021**, *31*, 635–637.

[14] Guo, X.; Fan, L. L.; Liu, Y. F.; Jin, Z. L. *In situ* XPS confirmed the efficient charge transfer of the CdS/GDY/$ZnMoO_4$ heterojunction based on graphdiyne(C_nH_{2n-2}) for photocatalytic hydrogen production. *Renew. Energy* **2024**, *222*, 119877.

[15] Man, R. W. Y.; Yi, H.; Malola, S.; Takano, S.; Tsukuda, T.; Häkkinen, H.; Nambo, M.; Crudden, C. M. Synthesis and

characterization of enantiopure chiral bis NHC-stabilized edge-shared Au_{10}-nanocluster with unique prolate shape. *J. Am. Chem. Soc.* **2022**, *144*, 2056–2061.

[16] Ruan, W. J.; Gao, Y.; Lin, J. H.; Fang, X. K. Polyoxometalate-dicarboxylate hybrid dimers with $\{SiW_{10}Cr_2\}$ nodes: Syntheses, structures, and mass spectrometric characterization. *Inorg. Chem.* **2024**, *63*, 12399–12403.

[17] Wang, Z.; Su, H. F.; Zhang, L. P.; Dou, J. M.; Tung, C. H.; Sun, D.; Zheng, L. S. Stepwise assembly of Ag_{42} nanocalices based on a Mo^{VI}-anchored thiacalix[4]arene metalloligand. *ACS Nano* **2022**, *16*, 4500–4507.

[18] Hu, Y. Q.; Zeng, M. H.; Zhang, K.; Hu, S.; Zhou, F. F.; Kurmoo, M. Tracking the formation of a polynuclear Co_{16} complex and its elimination and substitution reactions by mass spectroscopy and crystallography. *J. Am. Chem. Soc.* **2013**, *135*, 7901–7908.

[19] Zeng, M. H.; Yin, Z.; Liu, Z. H.; Xu, H. B.; Feng, Y. C.; Hu, Y. Q.; Chang, L. X.; Zhang, Y. X.; Huang, J.; Kurmoo, M. Assembly of a highly stable luminescent Zn_5 cluster and application to bio-imaging. *Angew. Chem., Int. Ed.* **2016**, *55*, 11407–11411.

[20] Liu, B.; Yu, F.; Tu, M.; Zhu, Z. H.; Zhang, Y. K.; Ouyang, Z. W.; Wang, Z.; Zeng, M. H. Tracking the process of a solvothermal domino reaction leading to a stable triheteroarylmethyl radical: A combined crystallographic and mass-spectrometric study. *Angew. Chem., Int. Ed.* **2019**, *58*, 3748–3753.

[21] Zhou, Y. L.; Zeng, M. H.; Wei, L. Q.; Li, B. W.; Kurmoo, M. Traditional and microwave-assisted solvothermal synthesis and surface modification of Co_7 brucite disk clusters and their magnetic properties. *Chem. Mater.* **2010**, *22*, 4295–4303.

[22] Cai, X.; Li, G. J.; Hu, W. G.; Zhu, Y. Catalytic conversion of CO_2 over atomically precise gold-based cluster catalysts. *ACS Catal.* **2022**, *12*, 10638–10653.

[23] Li, S.; Li, N. N.; Dong, X. Y.; Zang, S. Q.; Mak, T. C. W. Chemical flexibility of atomically precise metal clusters. *Chem. Rev.* **2024**, *124*, 7262–7378.

[24] Jiang, Z. G.; Zeng, H. M.; Zhang, X. Y.; Tan, Y.; Lan, Y. Z.; Wang, Y.; Long, D. L.; Cronin, L.; Zhan, C. H. A synergistic $\{Cu_2\text{-}W_{12}O_{40}\}$ catalyst with high conversion for homo-coupling of terminal alkynes. *Inorg. Chem. Front.* **2023**, *10*, 1255–1261.

[25] Wang, X. N.; Zhao, L. M.; Li, X. J.; Liu, Y.; Wang, Y. S.; Yao, Q. F.; Xie, J. P.; Xue, Q. Z.; Yan, Z. F.; Yuan, X. et al. Atomic-precision Pt_6 nanoclusters for enhanced hydrogen electro-oxidation. *Nat. Commun.* **2022**, *13*, 1596.

[26] Mitsuka, Y.; Ogiwara, N.; Mukoyoshi, M.; Kitagawa, H.; Yamamoto, T.; Toriyama, T.; Matsumura, S.; Haneda, M.; Kawaguchi, S.; Kubota, Y. et al. Fabrication of integrated copper-based nanoparticles/amorphous metal-organic framework by a facile spray-drying method: Highly enhanced CO_2 hydrogenation activity for methanol synthesis. *Angew. Chem., Int. Ed.* **2021**, *60*, 22283–22288.

[27] Zhang, B. X.; Chen, Y. P.; Wang, J. M.; Pan, H. G.; Sun, W. P. Supported sub-nanometer clusters for electrocatalysis applications. *Adv. Funct. Mater.* **2022**, *32*, 2202227.

[28] Xu, S. Y.; Shi, W. X.; Huang, J. R.; Yao, S.; Wang, C.; Lu, T. B.; Zhang, Z. M. Single-cluster functionalized TiO_2 nanotube array for boosting water oxidation and CO_2 photoreduction to CH_3OH. *Angew. Chem., Int. Ed.* **2024**, *63*, e202406223.

[29] Yang, Y.; Guo, S.; Zhang, Q.; Guan, Z. J.; Wang, Q. M. A cages-on-cluster structure constructed by post-clustering covalent modifications and guest-enabled stimuli-responsive luminescence. *Angew. Chem., Int. Ed.* **2024**, *63*, e202404798.

[30] Pan, Z. H.; Weng, Z. Z.; Kong, X. J.; Long, L. S.; Zheng, L. S. Lanthanide-containing clusters for catalytic water splitting and CO_2 conversion. *Coord. Chem. Rev.* **2022**, *457*, 214419.

[31] Chen, J. N.; Pan, Z. H.; Qiu, Q. H.; Wang, C.; Long, L. S.; Zheng, L. S.; Kong, X. J. Soluble Gd_6Cu_{24} clusters: Effective molecular electrocatalysts for water oxidation. *Chem. Sci.* **2024**, *15*, 511–515.

[32] Jirasek, M.; Sharma, A.; Bame, J. R.; Mehr, S. H. M.; Bell, N.; Marshall, S. M.; Mathis, C.; MacLeod, A.; Cooper, G. J. T.; Swart, M. et al. Investigating and quantifying molecular complexity using assembly theory and spectroscopy. *ACS Cent. Sci.* **2024**, *10*, 1054–1064.

[33] Sheng, K.; Wang, Z.; Li, L.; Gao, Z. Y.; Tung, C. H.; Sun, D. Solvent-mediated separation and reversible transformation of 1D supramolecular polymorphs built from $[W_{10}O_{32}]^{4-}$ templated 48-nuclei silver(I) cluster. *J. Am. Chem. Soc.* **2023**, *145*, 10595–10603.

[34] Wang, Z.; Li, L.; Feng, L.; Gao, Z. Y.; Tung, C. H.; Zheng, L. S.; Sun, D. Solvent-controlled condensation of $[Mo_2O_5(PTC4A)_2]^{6-}$ metalloligand in stepwise assembly of hexagonal and rectangular Ag_{18} nanoclusters. *Angew. Chem., Int. Ed.* **2022**, *61*, e202200823.

[35] Wang, Z.; Qu, Q. P.; Su, H. F.; Huang, P.; Gupta, R. K.; Liu, Q. Y.; Tung, C. H.; Sun, D.; Zheng, L. S. A novel 58-nuclei silver nanowheel encapsulating a subvalent Ag_{64}^{+} kernel. *Sci. China Chem.* **2020**, *63*, 16–20.

[36] Wang, Z.; Su, H. F.; Tan, Y. Z.; Schein, S.; Lin, S. C.; Liu, W.; Wang, S. A.; Wang, W. G.; Tung, C. H.; Sun, D. et al. Assembly of silver Trigons into a buckyball-like Ag_{180} nanocage. *Proc. Natl. Acad. Sci. USA* **2017**, *114*, 12132–12137.

[37] Wang, Z.; Zhu, Y. J.; Li, Y. Z.; Zhuang, G. L.; Song, K. P.; Gao, Z. Y.; Dou, J. M.; Kurmoo, M.; Tung, C. H.; Sun, D. Nuclearity enlargement from $[PW_9O_{34}@Ag_{51}]$ to $[(PW_9O_{34})_2@Ag_{72}]$ and 2D and 3D network formation driven by bipyridines. *Nat. Commun.* **2022**, *13*, 1802.

[38] Zheng, H. L.; Chen, X. L.; Li, T.; Yin, Z.; Zhang, Y. X.; Kurmoo, M.; Zeng, M. H. Manipulating clusters by use of competing N,O-chelating ligands: A combined crystallographic, mass spectrometric, and DFT study. *Chem.—Eur. J.* **2018**, *24*, 7906–7912.

[39] Zhang, Y. Y.; Zhang, D. S.; Li, T.; Kurmoo, M.; Zeng, M. H. *In situ* metal-assisted ligand modification induces Mn_4 cluster-to-cluster transformation: A crystallography, mass spectrometry, and DFT study. *Chem.—Eur. J.* **2020**, *26*, 721–728.

[40] Jiang, X.; Li, J.; Yang, B.; Wei, X. Z.; Dong, B. W.; Kao, Y.; Huang, M. Y.; Tung, C. H.; Wu, L. Z. A bio-inspired Cu_4O_4 cubane: Effective molecular catalysts for electrocatalytic water oxidation in aqueous solution. *Angew. Chem., Int. Ed.* **2018**, *57*, 7850–7854.

[41] Kim, Y.; Sridharan, A.; Suess, D. L. M. The elusive mononitrosylated $[Fe_4S_4]$ cluster in three redox states. *Angew. Chem., Int. Ed.* **2022**, *61*, e202213032.

[42] Olshansky, L.; Huerta-Lavorie, R.; Nguyen, A. I.; Vallapurackal, J.; Furst, A.; Tilley, T. D.; Borovik, A. S. Artificial metalloproteins containing Co_4O_4 cubane active sites. *J. Am. Chem. Soc.* **2018**, *140*, 2739–2742.

[43] Song, F. Y.; Moré, R.; Schilling, M.; Smolentsev, G.; Azzaroli, N.; Fox, T.; Luber, S.; Patzke, G. R. $\{Co_4O_4\}$ and $Co_xNi_{4-x}O_4$ cubane water oxidation catalysts as surface cut-outs of cobalt oxides. *J. Am. Chem. Soc.* **2017**, *139*, 14198–14208.

[44] Zeng, M. H.; Yao, M. X.; Liang, H.; Zhang, W. X.; Chen, X. M. A single-molecule-magnetic, cubane-based, triangular Co_{12} supercluster. *Angew. Chem., Int. Ed.* **2007**, *46*, 1832–1835.

[45] Ma, X. F.; Wang, Z. X.; Chen, X. L.; Kurmoo, M.; Zeng, M. H. Ligand effect on the single-molecule magnetism of tetranuclear Co(II) cubane. *Inorg. Chem.* **2017**, *56*, 15178–15186.

[46] Zhang, C. X.; Chen, C. H.; Dong, H. X.; Shen, J. R.; Dau, H.; Zhao, J. Q. A synthetic Mn_4Ca-cluster mimicking the oxygen-evolving center of photosynthesis. *Science* **2015**, *348*, 690–693.

[47] Berggren, G.; Adamska, A.; Lambertz, C.; Simmons, T. R.; Esselborn, J.; Atta, M.; Gambarelli, S.; Mouesca, J. M.; Reijerse, E.; Lubitz, W. et al. Biomimetic assembly and activation of [FeFe]-hydrogenases. *Nature* **2013**, *499*, 66–69.

[48] Gao, X. T.; Zhang, S.; Wang, P. T.; Jaroniec, M.; Zheng, Y.; Qiao, S. Z. Urea catalytic oxidation for energy and environmental applications. *Chem. Soc. Rev.* **2024**, *53*, 1552–1591.

[49] Huang, C. J.; Xu, H. M.; Shuai, T. Y.; Zhan, Q. N.; Zhang, Z. J.; Li, G. R. Modulation strategies for the preparation of high-performance

catalysts for urea oxidation reaction and their applications. *Small* **2023**, *19*, e2301130.

[50] Xu, S.; Ruan, X. W.; Ganesan, M.; Wu, J. D.; Ravi, S. K.; Cui, X. Q. Transition metal-based catalysts for urea oxidation reaction (UOR): Catalyst design strategies, applications, and future perspectives. *Adv. Funct. Mater.* **2024**, *34*, 2313309.

[51] Zhang, X.; Zhao, K.; Peng, X.; Kurmoo, M.; Zeng, M.H. *In-situ* evolution process understanding from a salan-ligated manganese cluster to supercapacitive application. *Nano Res.* **2022**, *15*, 346–351.

[52] Wang, Y. F.; Liang, Y. Y.; Wu, Y. F.; Yang, J.; Zhang, X.; Cai, D. D.; Peng, X.; Kurmoo, M.; Zeng, M. H. *In situ* pyrolysis tracking and real-time phase evolution: From a binary zinc cluster to supercapacitive porous carbon. *Angew. Chem. , Int. Ed.* **2020**, *59*, 13232–13237.

[53] Long, B. J.; Cao, P. Y.; Zhao, Y. M.; Fu, Q. Q.; Mo, Y.; Zhai, Y. M.; Liu, J. J.; Lyu, X.; Li, T.; Guo, X. F. et al. Pt_1/Ni_6Co_1 layered double hydroxides/N-doped graphene for electrochemical non-enzymatic glucose sensing by synergistic enhancement of single atoms and doping. *Nano Res.* **2023**, *16*, 318–324.

[54] Li, T.; Wang, Y. F.; Yin, Z.; Li, J.; Peng, X.; Zeng, M. H. The sequential structural transformation of a heptanuclear zinc cluster towards hierarchical porous carbon for supercapacitor applications. *Chem. Sci.* **2022**, *13*, 10786–10791.

[55] Zhao, J. Q.; Cai, D. D.; Dai, J.; Kurmoo, M.; Peng, X.; Zeng, M. H. Heptanuclear brucite disk with cyanide bridges in a cocrystal and tracking its pyrolysis to an efficient oxygen evolution electrode. *Sci. Bull.* **2019**, *64*, 1667–1674.

[56] Yu, Y. D.; Mu, Z.; Jin, B.; Liu, Z. M.; Tang, R. K. Organic–inorganic copolymerization for a homogenous composite without an interphase boundary. *Angew. Chem., Int. Ed.* **2020**, *59*, 2071–2075.

[57] O'Mullane, A. P. From single crystal surfaces to single atoms: Investigating active sites in electrocatalysis. *Nanoscale* **2014**, *6*, 4012–4026.

[58] Senthilkumar, N.; Gnana Kumar, G.; Manthiram, A. 3D hierarchical core–shell nanostructured arrays on carbon fibers as catalysts for direct urea fuel cells. *Adv. Energy Mater.* **2018**, *8*, 1702207.

[59] Qin, H. Y.; Ye, Y. K.; Li, J. H.; Jia, W. Q.; Zheng, S. Y.; Cao, X. J.; Lin, G. L.; Jiao, L. F. Synergistic engineering of doping and vacancy in $Ni(OH)_2$ to boost urea electrooxidation. *Adv. Funct. Mater.* **2023**, *33*, 2209698.

[60] Zhang, B. J.; Pan, C. T.; Liu, H. J.; Wu, X. S.; Jiang, H. J.; Yang, L.; Qi, Z. M.; Li, G.; Shan, L.; Lin, Y. X. et al. Achieving high-efficient urea oxidation via regulating the rate-determining step over a V single atom incorporated Co hydroxide electrocatalyst. *Chem. Eng. J.* **2022**, *439*, 135768.

[61] Zhang, L. S.; Wang, L. P.; Lin, H. P.; Liu, Y. X.; Ye, J. Y.; Wen, Y. Z.; Chen, A.; Wang, L.; Ni, F. L.; Zhou, Z. Y. et al. A lattice-oxygen-involved reaction pathway to boost urea oxidation. *Angew. Chem., Int. Ed.* **2019**, *58*, 16820–16825.

[62] Zhu, D. D.; Zhang, H. Y.; Miao, J. H.; Hu, F.; X. Wang, L. ; Tang, Y. J.; Qiao, M.; Guo, C. X. Strategies for designing more efficient electrocatalysts towards the urea oxidation reaction. *J. Mater. Chem. A* **2022**, *10*, 3296–3313.